



LAWRENCE
LIVERMORE
NATIONAL
LABORATORY

Plasticity Effects in Dynamically Loaded Nickel Aluminide Bicrystals

E. Loomis, D. Swift, J. McNaney, H. Lorenzana,
P. Peralta

December 4, 2008

Acta Materialia

Disclaimer

This document was prepared as an account of work sponsored by an agency of the United States government. Neither the United States government nor Lawrence Livermore National Security, LLC, nor any of their employees makes any warranty, expressed or implied, or assumes any legal liability or responsibility for the accuracy, completeness, or usefulness of any information, apparatus, product, or process disclosed, or represents that its use would not infringe privately owned rights. Reference herein to any specific commercial product, process, or service by trade name, trademark, manufacturer, or otherwise does not necessarily constitute or imply its endorsement, recommendation, or favoring by the United States government or Lawrence Livermore National Security, LLC. The views and opinions of authors expressed herein do not necessarily state or reflect those of the United States government or Lawrence Livermore National Security, LLC, and shall not be used for advertising or product endorsement purposes.

Plasticity Effects in Dynamically Loaded Nickel Aluminide Bicrystals

E. Loomis*, D. Swift*, J. McNaney[†], H. Lorenzana[†] and P. Peralta**

*P-24, Los Alamos National Laboratory, Los Alamos, NM 87544, USA

[†]Lawrence Livermore National Laboratory, Livermore, CA, USA

**Arizona State University, Tempe, AZ, USA

Abstract. Elastic and plastic anisotropy are believed to play large roles in the dynamic deformation of many materials at the grain-level. More importantly to polycrystalline materials is how velocity and stress perturbations are transmitted across interfaces in anisotropic materials. Very little work has been done in this area even though it is important for understanding shock/grain boundary interactions. Therefore, experiments have been performed using nanosecond laser shocks of grown Nickel Aluminide bicrystals at tens of GPa. Velocity histories were measured along a line on the back (free) surface of the bicrystals and used to characterize the material behavior. Unstable plastic flow in $\langle 100 \rangle$ grains was seen to occur when loaded above 700 m/s free surface velocity. Flow stresses in $\langle 111 \rangle$ and $\langle 100 \rangle$ grains were measured to be 2.9 and 3.3 GPa, respectively. Calculations were performed based on anisotropic elasticity and dislocation motion on primary slip systems to measure plastic flow properties where plastic strain-rates on the order of $10^6 s^{-1}$ were calculated using the experimental velocity histories. Definitive evidence of plastic wave scattering at the grain boundary was not observed experimentally; however, behavior across the grain boundary has been measured. The observations show that a smooth transition occurs between the elastic precursors in both grains as well as the plastic waves (when plastic flow is evident). An anisotropic elastic-plastic wave scattering model has been developed to explain the mechanisms affecting shock/grain boundary interactions.

Keywords: anisotropy, grain boundary, NiAl, plastic wave, refraction

PACS: 52.57.-z, 83.50.-v

1. INTRODUCTION

When materials exhibiting elastic and plastic anisotropy are dynamically loaded, different regimes of material behavior can be explored depending on the magnitude of the applied pressure. At pressures up to the elastic limit of the material, anisotropic elastic wave propagation governs the behavior, where the velocity of small perturbations is obtained by acoustic theory and the eigenvalues of the Christoffel tensor [1, 2]. In this regard, Loomis et al. [3] have established a connection between observed cracking and the envelope of elastic waves scattered from grain boundaries in shock loaded NiAl by using the slowness vectors extracted from the inverse of the Christoffel tensor.

Above the elastic limit a transition region exists where plastic deformation (dislocation slip, twinning, etc.) occurs and the elastic moduli (most importantly, the bulk modulus) increase with pressure. The range of pressures over which this region persists is material dependent.

A number of researchers have studied this regime through experimental and computational methods. Paisley et al. [4] and Loveridge-Smith et al. [5] have used Transient X-ray Diffraction (TXD) to measure the elastic-plastic response of silicon and copper during laser-induced shock compression. The experiments on copper have shown it to have almost equal Bragg and

Laue diffraction, which indicates that it undergoes almost completely hydrostatic compression when shocked along [100]. In contrast, silicon displays no change in Laue signal to surprisingly high pressures when shocked along the [100] direction, showing it to have a purely elastic response [5]. Swift et al. [6] made simultaneous free surface velocity measurements and TXD measurements of shock loaded beryllium. From these experiments, differences in flow stress in single and polycrystalline samples were observed as well as differences in wave structures where a sharp drop-off in velocity was found prior to plastic wave arrival in [0001] samples.

To begin to understand the mechanisms of some of the observed behavior seen experimentally, a number of authors have attempted to model dynamic plasticity. Propagation speeds of plastic wave fronts have been calculated on a theoretical basis by Craggs [7], Ting et al. [8], and various other authors under the assumptions of isotropic elasticity and various plastic constitutive relations. Here the anisotropic plastic response has been shown to be dependent on the normal to the yield surface. Reddy and Gulup [9] have also investigated plastic wave speeds and contributed to research on propagating plastic loading/unloading boundaries for finite deformations and a general plastic flow law. A lack of understanding, however, still remains as far as how the spherical part of the stress state and the deviatoric part (through which plas-

ticity acts) contribute to the overall material response for increasing compression up to the overdrive pressure and full hydrodynamic behavior.

An even lower level of understanding exists for material behavior when microstructural defects such as grain boundaries are introduced into the path of these plastic waves. Cizek and Ting [10] as well as Jahsman [11] have approached this problem from the theoretical basis of what are termed "acceleration waves" where the lowest order discontinuities across a propagating wave front are only in the temporal and spatial derivatives of the velocity and stress. Their analyses were performed only considering reflection of elastic-plastic waves from rigid or free surfaces and relatively simple rate independent hardening laws such as perfect plasticity or linear hardening. Although the theories posed in these papers are a satisfactory start and valuable insight is gained into basic plastic wave reflection behavior, little use can be made of them when considering real crystalline materials.

Little to no experimental research has been performed to directly investigate plastic wave behavior in the vicinity of a grain boundary to fill the shortcomings of theoretical research in these areas. For this reason, we have performed laser shock experiments on bicrystals of the intermetallic compound Nickel Aluminide (NiAl). An analysis of the free surface velocity measurements has been performed as well as simulations of the laser ablation process with a radiation hydrodynamics code. The next section discusses the methods undertaken to measure shock/grain boundary interactions in crystalline materials.

2. EXPERIMENTAL PROCEDURE

NiAl was chosen for these experiments for various reasons. In particular, it displays elastic and plastic anisotropy (it plastically deforms on well known slip planes and directions (primarily $\{110\}\langle 001 \rangle$) [12, 13, 14, 15]) and it is a stable material to grow in single crystal form. This last property is very important to the sample preparation aspects of this research. We believed it to be necessary to have as close to true grain boundaries as possible as an interface for our samples since processes such as diffusion bonding can introduce defects and gradients in the material properties not normally found in real materials thus altering the actual response. For this reason, bicrystals were grown using standard single crystal growth techniques, as detailed next.

2.1. Bicrystal Growth

Variations in elastic and plastic properties across a grain boundary was seen to produce localized strain at the intersection of the grain boundary and free surface in simulations by Greening and Koskelo [16]. In an attempt to observe similar behavior experimentally, shock experiments were performed on samples containing two differently oriented grains separated by an inclined grain boundary (bicrystal). High purity single crystals of stoichiometric NiAl were supplied by GE Aircraft Engines. Two single crystals were cut with a wire electro-discharge machine (EDM) into half cylinders so that the cut plane was parallel with the desired crystallographic plane. One of the crystals had a $\langle 110 \rangle$ direction along the cylinder axis and the cut plane was roughly 9 degrees from another $\langle 110 \rangle$ direction. The second single crystal had a $\langle 100 \rangle$ direction along the cylinder axis and a cut plane parallel with a $\langle 110 \rangle$ direction. These orientations were chosen so that the resulting bicrystal once cut into the final sample geometry would have a $\langle 100 \rangle$ loading axis in one grain and a $\langle 111 \rangle$ loading axis in the other grain separated by a 45 degree inclined boundary. This orientation also maximized the difference in longitudinal elastic wave speed as well as the difference in flow stress. A dual halogen optical floating zone unit was used for bicrystal growth as shown in Fig. 1.

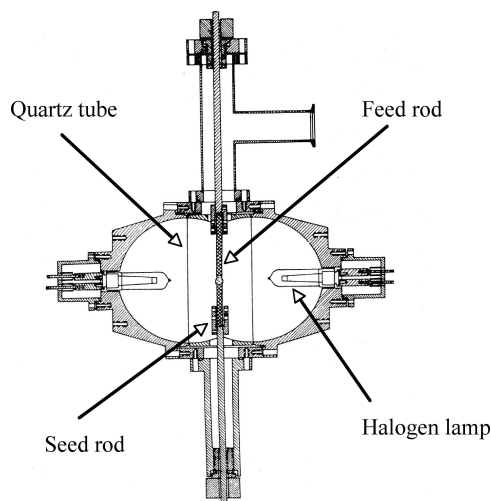


FIGURE 1. Optical floating zone unit used for crystal growth

In this technique, the cut planes of the two oriented single crystals are placed together and set inside a fixture at the bottom of the unit. A parallelepiped of polycrystalline NiAl is hung from another fixture directly above the two single crystal seeds and acts as a "feed rod" to supply material for the growth process. A zone of molten material is formed by focusing light from the halogen lamps to a point at the top of the two single crystals.

The feed rod is then brought into contact with the molten material forming an interface between the single crystal seeds and polycrystalline NiAl. The molten zone is then moved upwards at about 20 mm/hr relative to the downward moving seeds and feed rod, which results in a solidifying bicrystal attached to the two single crystal seeds. The seeds and feed rod are counter-rotated to stabilize the growth and to create a uniform temperature gradient around the circumference of the melt. The process is completed after the end of the feed rod is reached or the grain boundary wanders too far to one side. One bicrystal grown with this technique is shown in Fig. 2.

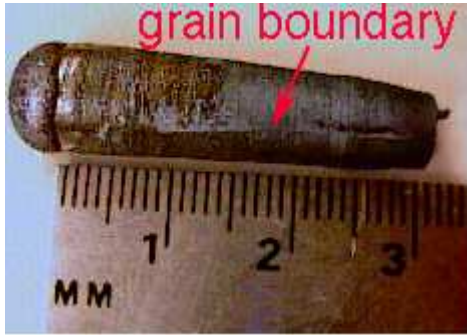


FIGURE 2. NiAl bicrystal grown with optical floating zone technique prior to sectioning

Sections were extracted from this bicrystal by locating the desired $\langle 111 \rangle$ and $\langle 100 \rangle$ planes in the two grains with back reflection Laue x-ray diffraction. 500 micron thick sections were cut from the length of the grown bicrystal so that the $\langle 111 \rangle$ and $\langle 100 \rangle$ planes were parallel with the sample plane in each grain. The length of the cuts was about 5 mm resulting in nearly rectangular sample geometries with dimensions $5 \times 7 \times .5$ mm. The samples were then polished down to between 160 and 270 microns thick with both sides close to mirror finishes. The mean grain boundary inclination was measured at 6 sections along the length of the original bicrystal for post-shock analysis and simulation.

Orientation imaging microscopy (OIM) was then performed to verify the orientations of each grain. Fig. 3 shows the inverse pole figure (crystallographic direction corresponding to the surface normal) in the grain boundary region of one of the polished surface along with the inverse pole figure key.

2.2. Laser shock compression

Shock loading experiments were performed using the JANUS laser at Lawrence Livermore National Laboratory. Lasers used for this type of testing are typically capable of delivering hundreds of joules over ones to tens of nanoseconds in the form of 527 nm (green) laser light.

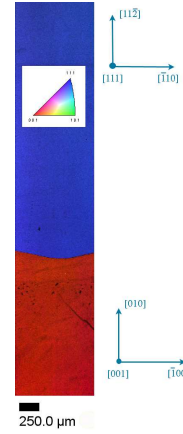


FIGURE 3. Inverse pole figure map showing the $\langle 111 \rangle$ and $\langle 001 \rangle$ orientations of each bicrystal sample

The irradiance delivered to the target was then adjusted by focusing/defocusing the drive beam to different spot sizes on the target surface. Temporal pulse shaping was done to tailor the loading history inside the target. The shaped pulse was then sent through an array of disk and rod amplifiers to obtain the desired total energy for each shot.

Large changes to the ablation pressure were achieved by adjusting the diameter of the main drive beam while finer changes were made by adjusting the total energy prior to each shot. Laser spot sizes were measured following any adjustment to the main focusing lens by monitoring an alignment pulse with a CCD camera. The temporal shape of the drive pulse was approximately ramped from 70 to 100 % over 10 ns and recorded along with the total energy during each shot by passing a fraction of the pulse into a photodiode. The pulse histories for three shots are shown in Fig. 4.

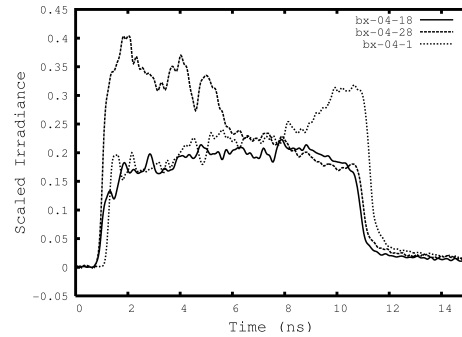


FIGURE 4. Example laser pulse shapes from bicrystal experiments

From previous experiments and simulations, we found that the 70-100 % ramping of the drive pulse produces flat topped pressure profiles for 2.4 ns laser pulses. Difficulties were encountered in getting the desired ramped

pulse shapes following large changes to the drive energy, which produced some unexpected and undesired loading histories as seen in sample bx-04-28 of Fig. 4. These loadings histories did not appear to drastically alter the loading as will be shown in the radiation hydrodynamics simulations and experimental velocity records.

Free surface velocity measurements were made during each shot using two Velocity Interferometry Systems for Any Reflector (VISAR). Light from an incident probe laser was reflected off the back surface of the target and then split and fed into each of the VISAR's. The interferometers were of the Mach-Zehnder type where the reflected light was sent through two different optical paths one of which contained a delay etalon to shift in time the light passing through one leg relative to the other before recombining the two. The interference pattern was then fed into the slit of an optical streak camera to record the free surface motion. For these experiments, we used etalons with different fringe constants for each VISAR so that one VISAR would record large scale motion while the other would record small scale changes. The calculated velocity-per-fringe (VPF) for each etalon was 497 m/s/fringe and 1238 m/s/fringe so that one full fringe shift recorded with the streak camera was equal to 497 m/s and 1238 m/s respectively. A timing pulse was also fed into one of the streak cameras to accurately measure the time of shock breakout at the free surface. Fig. 5 shows a schematic cross-section of a bicrystal target, laser drive, and VISAR. The statistics

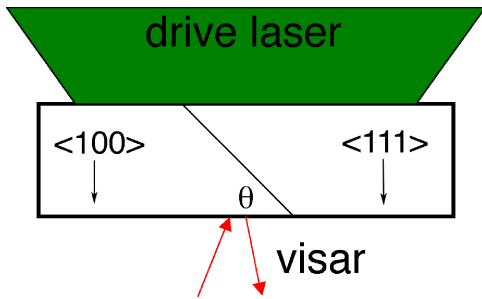


FIGURE 5. Schematic of bicrystal experiments showing drive laser, grain boundary inclination, and diagnostics

for each shot in the bicrystal series are given in Table 1. Three sets of bicrystal targets were shot under reversed directions by which we mean the targets were flipped so that the propagating shock made a $\langle 100 \rangle$ to $\langle 111 \rangle$ transition across the boundary instead of a $\langle 111 \rangle$ to $\langle 100 \rangle$ transition. The shock transition for each sample is shown in table 1 under the column "orientation". In this column the first direction gives the grain in which the shock was initiated (in the grain boundary region) and the second direction gives the grain in which the shock was refracted into after crossing the boundary. It was believed that differences in plastic wave behavior would occur due to the transition between a low flow stress $\langle 111 \rangle$

grain and a high flow stress $\langle 100 \rangle$ grain. Specifically, for different applied pressures we would expect to see a plastic-plastic transition, a plastic-elastic transition, an elastic-plastic transition, or an elastic-elastic transition. The nominally 1 mm diameter probe laser allowed us to make bulk plastic wave measurements along with grain boundary interactions.

3. LASER ABLATION SIMULATIONS USING RADIATION HYDRODYNAMICS

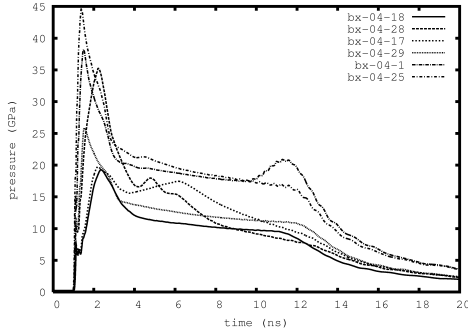
Knowledge of the actual loading histories was desired for these experiments so that accurate continuum mechanics simulations could be performed. However, the physics of laser-matter interactions is a complex process requiring the use of good radiation hydrodynamics codes. The code used to simulate the laser ablation in these experiments was Hyades [Cascade Applied Sciences, Inc.].

A 527 nm laser source was used as the applied energy to one side of a one-dimensional mesh with the opposite surface of the mesh free. The laser irradiance as a function of time was inserted in tabular form based on the in-situ measured laser drive history for each shot. The Thomas-Fermi ionization model [17] was used to calculate the free electron density and material properties were specified through equation of state (EOS) and Rosseland (and Planck) group mean opacity tables where the EOS tables were constructed from first principles by Swift [18]. The mesh itself was 80 microns long and consisted of 300 elements increasing in size toward the free surface by 2.5 %. The mesh consisted of two regions governed by two different equations of state. The first region was limited to the first 5 microns from the energy deposition surface and was modeled by a free atomic gas made up of an equal number of nickel and aluminum atoms to represent the ablating plasma and a solid EOS was used to describe the behavior in the remainder of the mesh. The simulations were run for 25 ns and the resulting pressure histories at 5 microns from the energy deposition surface were extracted and are shown in Fig. 6.

As the graph in Fig. 6. shows, the highest pressures were confined to about the first 3 ns in the drive. Following the peak, the pressure dropped to a somewhat constant level for about 10 ns then decayed somewhat slowly down to zero. Early time oscillations were encountered in the solution and were most likely brought on by the presence of the plasma/solid interface used in these simulations, which created an impedance mismatch and thus reflections of shock waves back into the plasma. This interface is not perfect in reality and probably has a finite thickness where the properties change from plasma to solid more smoothly; however, it is nec-

TABLE 1. Target, laser, and VISAR parameters for each bicrystal experiment ($t_0=937$ ns)

target			laser			VISAR
sample	orientation	thickness (microns)	timing f ducial (ns)	spot size (mm)	energy (J)	sweep (ns)
bx-04-18	$\langle 111 \rangle / \langle 100 \rangle$	165	t_0+10	4	308	50
bx-04-28	$\langle 100 \rangle / \langle 111 \rangle$	175	t_0+10	4	463	50
bx-04-17	$\langle 100 \rangle / \langle 111 \rangle$	165	t_0+20	4	396	20
bx-04-29	$\langle 111 \rangle / \langle 100 \rangle$	160	t_0+25	4	397	20
bx-04-1	$\langle 100 \rangle / \langle 111 \rangle$	160	t_0+20	3	414	20
bx-04-25	$\langle 111 \rangle / \langle 100 \rangle$	210	t_0+25	3	433	20

**FIGURE 6.** Pressure histories of bicrystal targets from radiation hydrodynamic simulations

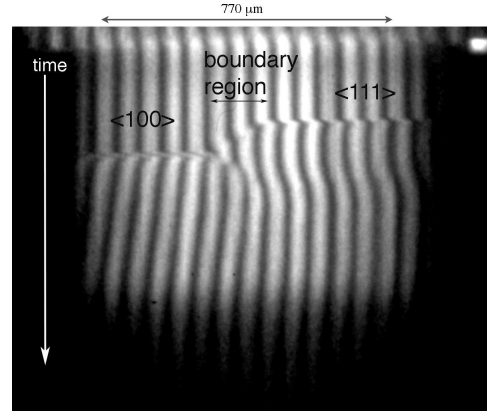
essary in order to model the material behavior in both the plasma and solid states since a wide ranging EOS is not yet available for NiAl. The amplitude of the oscillations decreased with increasing plasma layer thickness. The 5 micron thick plasma layer used in these simulations was chosen because this value minimized the early time oscillations and kept the plasma layer thickness closest to its true value of about 2 microns (this value corresponds to the end of the ablation zone in the simulations).

4. ANALYSIS OF FREE SURFACE VELOCITY MEASUREMENTS

From these experiments, numerous sets of interesting plastic (and elastic) wave data can be extracted including orientation dependent precursor velocities, pressure dependent plastic wave and particle velocities, single crystal flow stresses, as well as the grain boundary effects mentioned above and the overall size of the grain boundary affected zone (GBAZ). In this section we will discuss some of these results for each shocked bicrystal.

The VISAR record for sample bx-04-18 is shown in Fig. 7.

In the VISAR records that follow, the horizontal direction represents the position along the VISAR line on the back surface of the sample and time advances vertically

**FIGURE 7.** Line VISAR record for sample bx-04-18

downward. The fringe constant for all records of this type is 497 m/s/fringe (increasing velocity is a shift to the right). The bright spot in the upper right hand corner is the timing f ducial used for measuring shock arrival. A fringe following algorithm was used to extract actual velocity data by fitting a cosine function to the maxima and minima of the static fringe record then manually following the moving fringes by selecting many points along each one. For each VISAR record, graphs have been constructed showing each of the three regions (bulk of $\langle 100 \rangle$ grain, bulk of $\langle 111 \rangle$ grain, and grain boundary region) separately. These graphs for sample bx-04-18 are shown in Fig. 8.

From Fig. 8 (a) we see that a free surface velocity of roughly 500 m/s was achieved in the bulk of the $\langle 100 \rangle$ grain, which equates to 250 m/s particle velocity after correcting for velocity doubling. No indication of a plastic wave is found in the bulk of this grain. The $\langle 111 \rangle$ grain on the other hand shows a significant increase in particle velocity around 30 ns after the initiation of the drive pulse indicating the arrival of a plastic wave front. The precursor velocity is about 225 m/s (≈ 110 m/s particle velocity), which gives a measure of the flow stress for $\langle 111 \rangle$ crystals. The flow stress can be calculated from the particle velocity by assuming a von Mises yield criterion and uniaxial straining in the shock

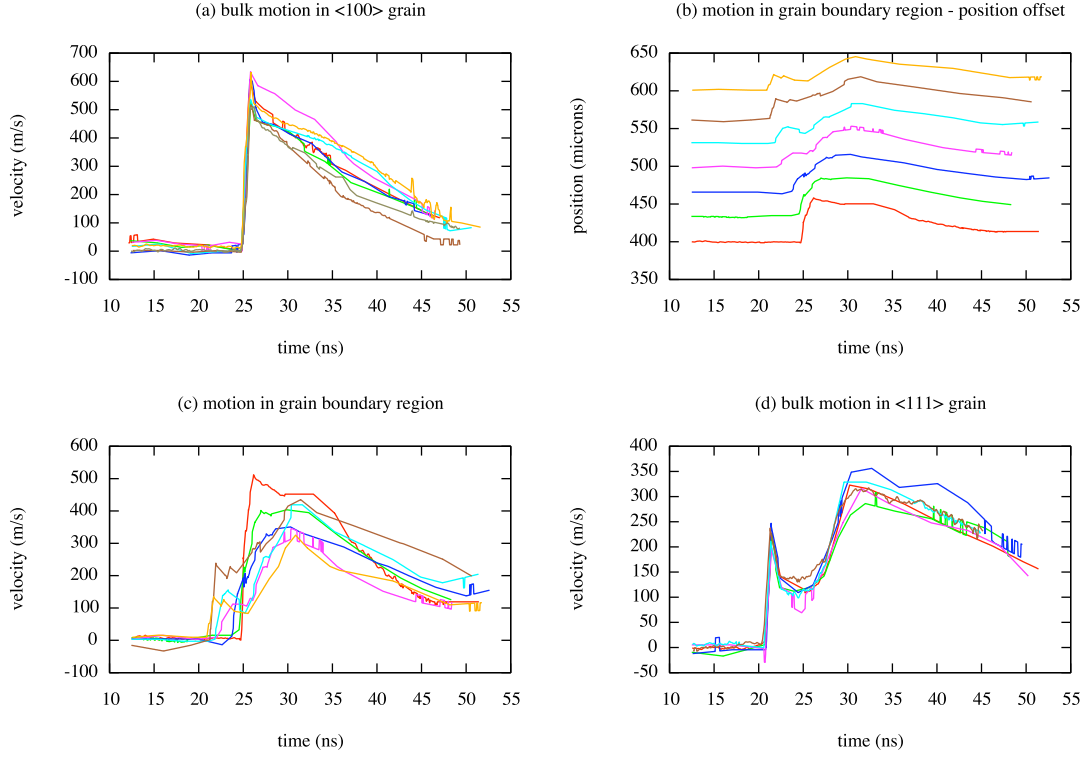


FIGURE 8. Analyzed velocity records for sample bx-04-18 showing various regions of bicrystal

direction. The flow stress is then calculated by

$$Y = \frac{3}{2} \sigma_{11} \left(1 - \frac{c_b^2}{c_l^2} \right) \quad (1)$$

where $\sigma_{11} = 1/2 \rho c_l u_f$, $c_l^2 = C_{1111}/\rho$, and $c_b^2 = K/\rho$. The parameters to be inserted into (1) are given in table 2. Inserting the wave speeds into (1) gives 2.9 GPa for the <111> crystal.

A significant stress relaxation process took place prior to plastic wave arrival where the free surface velocity dropped to about 125 m/s during the transition of the material into the plastic state. The free surface velocity then rose to about 300 m/s behind the plastic wave front. Stress relaxation and precursor decay have been observed in a number of materials such as LiF [19, 20] and Aluminum [21]. In these studies the primary focus was on precursor decay where significant reductions in precursor amplitude were observed over millimeters. Dislocation nucleation and multiplication and hydrodynamic decay were given as the primary causes of precursor decay. It appears as though similar mechanisms are responsible for stress relaxation immediately behind the precursor the most important being multiplication of dislocations by cross-slip. Stress relaxation has even been

observed in quasi-static compression tests of single crystal NiAl [15].

Figure 8 (b) shows the approximate position over which the grain boundary affected the material response to the incident shock by plotting the position of the fringes in the grain boundary region as a function of time. This shows that a region was affected by the inclusion of the grain boundary on the order of 200 microns, which is greater than the roughly 140 micron long boundary trace on any surface parallel to the free surface. This means that waves had to scatter upon interacting with the grain boundary. The scattering process would have resulted in elastic waves changing direction and thus velocity in a manner defined by the elastic constants on either side of the grain boundary [3]. It appears from the VISAR record that the region affected by the interaction of the plastic wave with the grain boundary is about the same as that of the elastic wave.

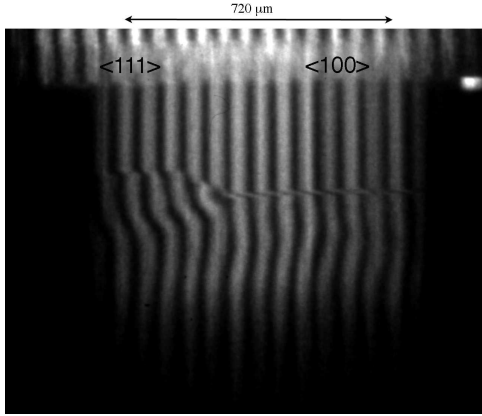
Figure 8 (c) has the same color coding as (b), but now the axes have changed to show velocity inside the grain boundary affected zone (GBAZ). From graph (c) we see a rather smooth transition between the precursor in the <100> grain and both the precursor and plastic wave front in the <111> grain. This structure can also be seen in (b). This is to be expected since in the grain boundary region, incident waves traveled partially through the

TABLE 2. NiAl elastic constants (contracted notation), density and wave speeds

Elastic constants (GPa)				density (kg/m ³)	wave speeds (m/s)		
C_{11}	C_{12}	C_{44}	K	ρ	c_b	c_{111}	c_{100}
200.65	133.23	114.48	155.7	5850	5200	7220	5856

fast elastic wave and low flow stress $\langle 111 \rangle$ grain and partially through the slow elastic wave and high flow stress $\langle 100 \rangle$ grain. The amount in which waves traveled in each grain varies linearly according to the roughly 45 degree grain boundary inclination.

Sample bx-04-28 was shot at a higher total energy than sample bx-04-18 to observe plastic wave behavior at a moderately higher pressure. The VISAR of this sample is shown in Fig. 9.

**FIGURE 9.** Line VISAR record for sample bx-04-28

The $\langle 111 \rangle$ elastic precursor is seen to arrive prior to the precursor in the $\langle 100 \rangle$ grain owing to the higher elastic wave speed along the $\langle 111 \rangle$ direction in NiAl. A noticeable plastic wave is again seen in the $\langle 111 \rangle$ grain. In the $\langle 100 \rangle$ grain, we possibly see the onset of a low amplitude plastic wave followed by release, which differs from sample bx-04-18. This wave structure can better be seen in the graphs of Fig. 10.

Graphs (a) and (d) of Fig. 10 show a 4 to 5 ns difference in precursor arrival times in the bulks of each grain. The free surface velocity behind the $\langle 100 \rangle$ precursor is about 525 m/s (260 m/s particle velocity). The free surface velocity then rises to about 575 m/s according to fringes in the bulk. The free surface velocity behind the plastic wave front in the $\langle 111 \rangle$ grain rises to about 425 m/s, which is significantly higher than sample bx-04-18. In the grain boundary region, a similar transition to that of sample bx-04-18 is seen between the bulk behaviors of the two grains.

The free surface velocity record of sample bx-04-17 is shown in Fig. 11. This sample was shot under reversed loading with respect to sample bx-04-18 for the reasons discussed in section 2. The first difference we see in

the VISAR records for each of these samples is that bx-04-17 shows a large velocity gradient between two bright fringes near the intersection of the grain boundary region and the bulk of the $\langle 100 \rangle$ grain in the form of a dark circular region. This region is clearly seen between the light blue and yellow curve in graphs (b) and (c) of Fig. 12. This signifies a very large velocity difference between two locations on either side of the grain boundary where it meets the free surface. These large spatial variations in velocity arise at this particular time because the particle velocity in the $\langle 100 \rangle$ grain is equal to the large precursor amplitude of 300 m/s and just on the other side of the boundary it is equal to roughly 100 m/s since the $\langle 111 \rangle$ plastic wave has yet to arrive.

Another interesting difference between the free surface velocities of this sample and bx-04-18 is that the structure of the precursor in the grain boundary region of this sample has a much more gradual slope whereas the same region in bx-04-18 shows a very steep slope. It is unclear if this structure is real or just an artifact of the interferometer due to the fringe shift direction being in the direction towards or away from increasing velocity in the spatial direction. Unfortunately, the streak camera triggered too early so later time behavior was missed.

Sample bx-04-29 was shot under load reversal with respect to sample bx-04-28. The VISAR record for this sample is shown in Fig. 13. Similar differences in the VISAR records of samples bx-04-29 and bx-04-28 as those of samples bx-04-17 and bx-04-18 such as the gap between two successive bright fringes near the intersection of the $\langle 100 \rangle$ grain and the grain boundary region. These gaps are seen in both samples bx-04-28 and bx-04-17 and not in bx-04-29 or bx-04-18. Figure 14 shows the free surface behavior in velocity-time and position-time space.

Graph (b) of Fig. 14 shows what is obviously an artifact of the interferometer where the precursor in the grain boundary region appears to move backward in time. The cause of this behavior comes from fringe shifts in the direction of large spatial gradients in velocity. The bulk behavior in this sample is similar to that of the previous samples, as expected, since these samples were shot under similar conditions with only moderate differences in total drive energy and small differences in sample thickness. Under these conditions, we seem to be on the verge of observing a $\langle 100 \rangle$ plastic wave on the back surface. In an attempt to study $\langle 100 \rangle$ plastic wave behavior, the next set of samples were tested at much

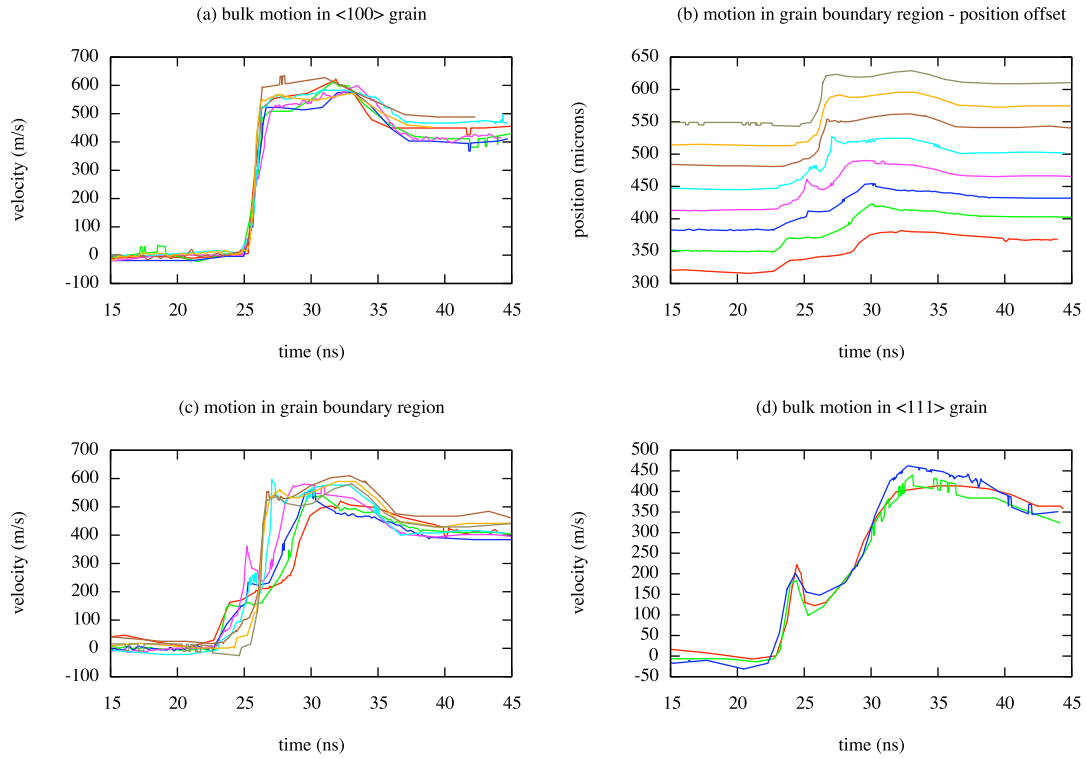


FIGURE 10. Analyzed velocity records for sample bx-04-28 showing various regions of bicrystal

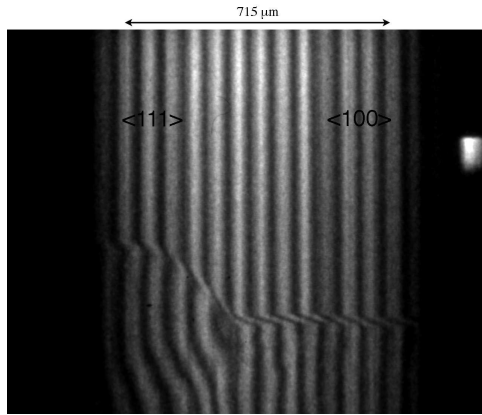


FIGURE 11. Line VISAR record for sample bx-04-17

higher irradiances and thus higher pressures.

Sample bx-04-1 was the first of these higher pressure samples and its corresponding free surface velocity record is shown in Fig. 15. A definite wave structure can be seen behind the precursor in the $\langle 100 \rangle$ grain, which appears rather jagged in comparison to the $\langle 111 \rangle$ structure. The average behavior behind the $\langle 100 \rangle$ precursor does result in a plastic wave with a peak free surface

velocity of around 1200 m/s as shown in Fig. 16. The $\langle 100 \rangle$ precursor amplitude is roughly 700 m/s (350 m/s particle velocity), which from eq. (1) results in a low stress of 3.3 GPa. The behavior behind the $\langle 100 \rangle$ precursor is a very interesting result. This appears to be the only region in which a smooth transition from elastic to plastic behavior did not occur. Instead, the material responded with several sharp transitions to higher velocity until it reached a maximum. These sharp transitions most likely correspond to the "kinking" mechanism known to occur in quasi-statically loaded $\langle 100 \rangle$ NiAl single crystals [12, 13, 14]. Since the primary slip direction in NiAl is $\langle 001 \rangle$ the Schmid factor for the primary slip system goes to zero as the $\langle 100 \rangle$ loading direction is approached, however for slight variations from $\langle 100 \rangle$ loading, the critically resolved shear stress for the primary system may still be lower than for any secondary systems. In this case, the resolved shear stress on the primary system can build up until it reaches the critical level where the stress will then be relieved in a quick burst of dislocation motion. This process will then repeat itself periodically.

It does appear that some stress relaxation occurred immediately behind the $\langle 100 \rangle$ precursor although not to the extent of the $\langle 111 \rangle$ grain. The ringing appears to first be perturbations on top of this stress relaxation

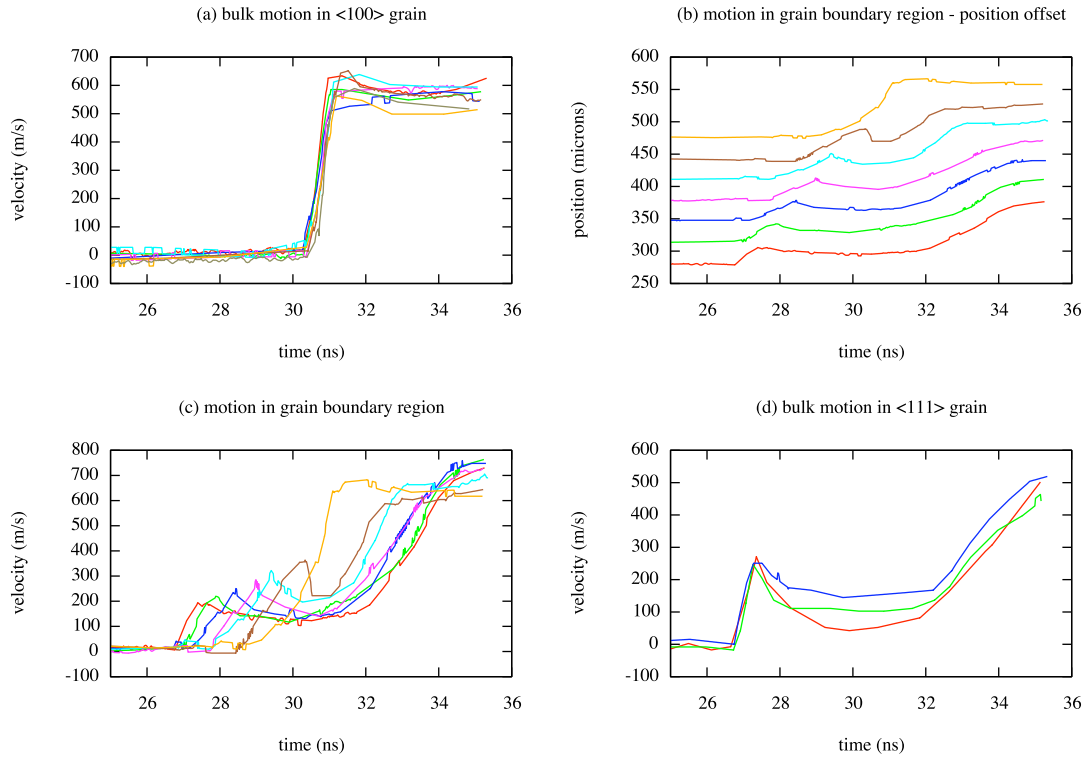


FIGURE 12. Analyzed velocity records for sample bx-04-17 showing various regions of bicrystal

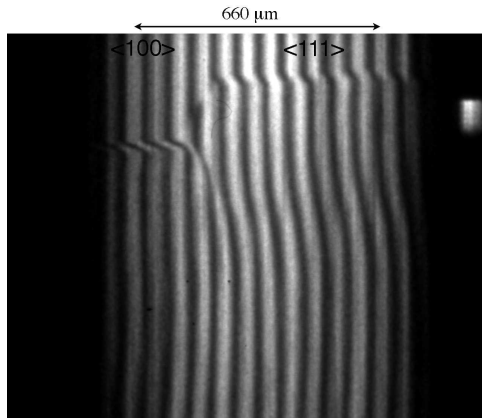


FIGURE 13. Line VISAR record for sample bx-04-29

where it then dominates the behavior once the particle velocity begins to again rise to its peak. The "ringing" also does not appear to be uniform across the $\langle 100 \rangle$ grain. This behavior differs significantly from the $\langle 111 \rangle$ grain where steady plastic flow occurred throughout the deformation process following the precursor. In the grain boundary region, there appears to be a transition between both the bulk precursors and the bulk plastic waves.

The magnitudes of the precursors do not seem to have a linear relationship with position (or time) across the grain boundary region as seen clearly in Fig. 16 (c). Near the $\langle 111 \rangle$ grain, the precursor amplitudes increase slowly until the $\langle 100 \rangle$ side is approached where a much sharper increase is found. The transition between the plastic waves is subtler than the transition between the precursors. The plastic wave transition appears to behave differently than that of the precursor transition where the time between the precursor and the plastic wave front is shortest about where the precursor transition begins on the $\langle 100 \rangle$ side (about at the fringe that starts at 550 microns on Fig. 16 (b)). On either side of this point, the time between the precursor and the plastic wave front increases.

Sample bx-04-25 was shot under similar conditions to that of bx-04-1 except this sample was about 50 microns thicker. The VISAR record for this sample is shown in Fig. 17.

The added thickness of this target seems to have been enough to smooth and diminish the plastic "ringing" observed in bx-04-1 through plastic and hydrodynamic decay since only a slight plastic wave is visible. A similar transition to that of sample bx-04-1 between the bulk plastic wave behavior of the $\langle 100 \rangle$ and $\langle 111 \rangle$ grains is seen clearer in this sample as Fig. 18 shows.

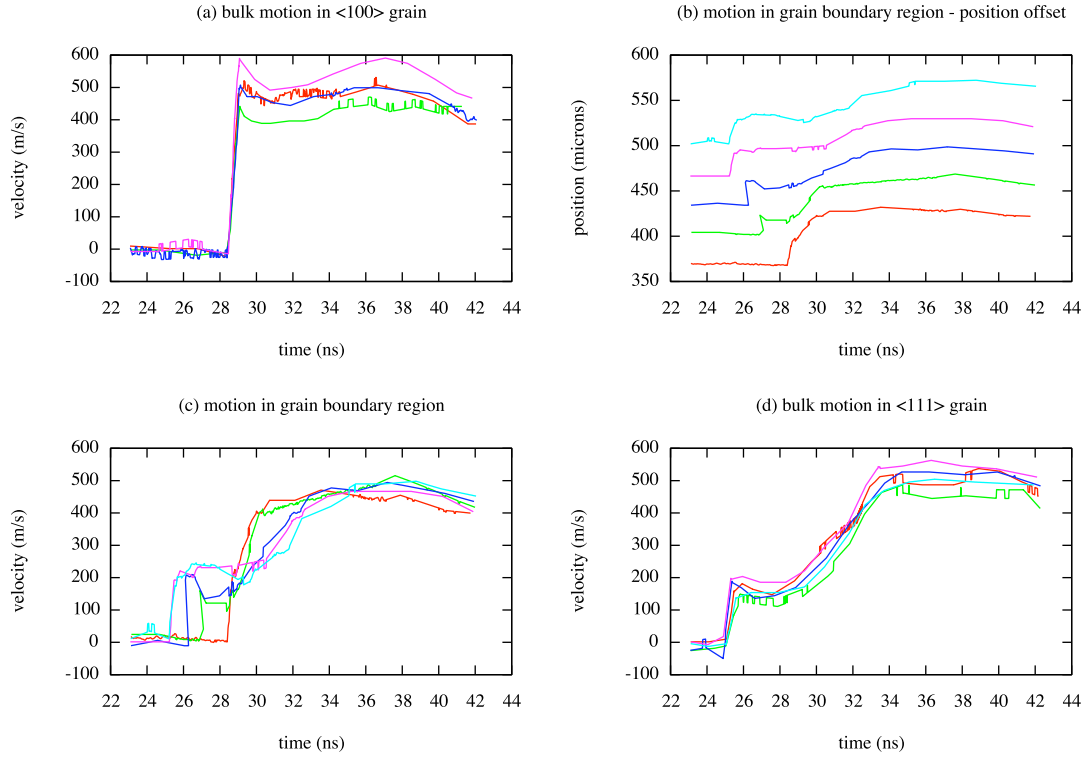


FIGURE 14. Analyzed velocity records for sample bx-04-29 showing various regions of bicrystal

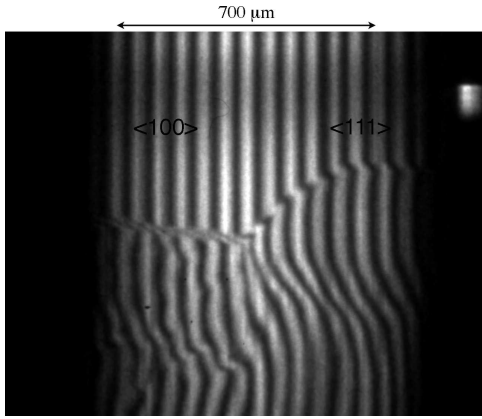


FIGURE 15. Line VISAR record for sample bx-04-1

Sample bx-04-25 appears to contain some grain boundary effects closer to the bulk of the $\langle 100 \rangle$ grain in the form of possible scattered plastic waves since a disturbance can be seen originating behind the precursors in the grain boundary region, which propagates to the left as time increases.

5. ANALYTICAL REPRESENTATION OF ELASTIC-PLASTIC WAVE PROPAGATION IN SINGLE CRYSTALS

To model grain boundary interactions in elastic-plastic wave problems goes beyond the scope of the current paper due to the fact that the problem is inherently unsteady in time and space and requires significant modeling (possibly numerical) efforts to treat the evolving scattering problem. Here we will only focus on the bulk response and retain the single crystal plasticity nature of the problem. Johnson [22] was the first to treat anisotropic elastic-plastic wave propagation using the kinematics of slip. Some approximations were used in that paper including isotropic elasticity and the use of a constant resolved shear stress throughout the deformation. The basic characteristics of elastic-plastic wave propagation were displayed such as the development of shear components due to anisotropic plasticity given an initially longitudinal disturbance. In this section we derive relatively simple relations to model the anisotropic behavior observed in the bulk of the VISAR records discussed in the previous section.

Under the assumption of small strain kinematics, the

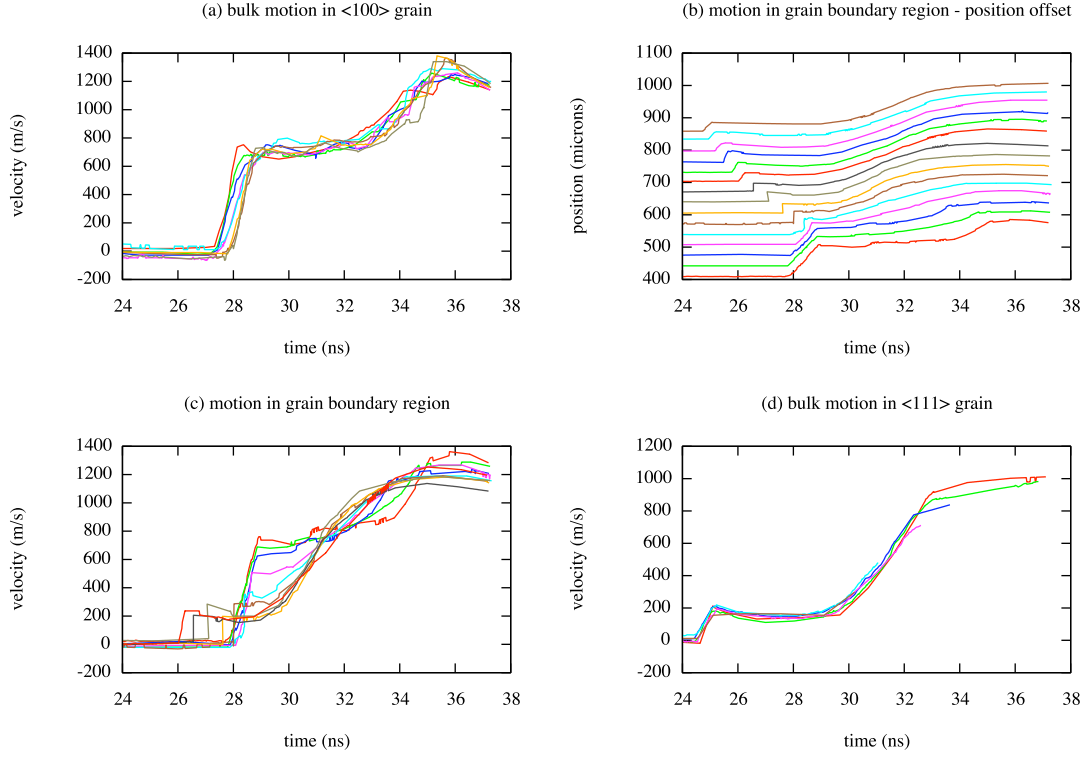


FIGURE 16. Analyzed velocity records for sample bx-04-1 showing various regions of bicrystal

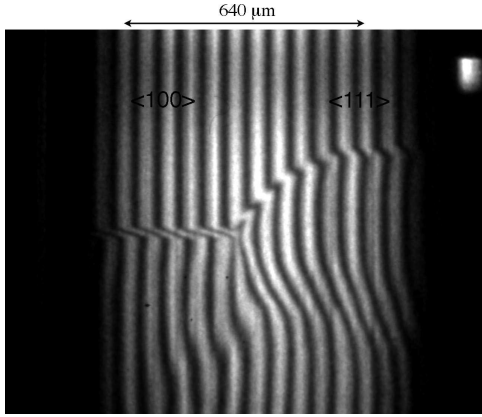


FIGURE 17. Line VISAR record for sample bx-04-25

additive decomposition of the strain-rate tensor is given by

$$\dot{\epsilon}_{ij} = \dot{\epsilon}_{ij}^e + \dot{\epsilon}_{ij}^p = \frac{1}{2}(v_{i,j} + v_{j,i}) \quad (2)$$

where $v_{i,j}$ is the velocity gradient. The relaxation of elastic deformation by plastic flow is described by

$$\dot{\sigma}_{ij} = C_{ijkl}(\dot{\epsilon}_{ij} - \dot{\epsilon}_{ij}^p) \quad (3)$$

where C_{ijkl} is the elastic stiffness tensor. Following Hill [23] and Janssen et al. [24], the gradient of a field in the neighborhood of a propagating hypersurface can be put in terms of the propagation velocity of the surface, the time derivative of the field, and the normal to the surface as

$$|v_{i,j}| = -\frac{1}{c}|\dot{v}_i|n_j \quad (4)$$

where $|\cdot|$ represents a jump in that quantity. Eq. (4) can be used in general for all rank tensors including the velocity and stress tensor. The equation of motion across the hypersurface in terms of time derivatives only is given by

$$|\dot{\sigma}_{ij}|n_j + \rho c|\dot{v}_i| = 0 \quad (5)$$

Assuming jumps in all fields, we now drop the $|\cdot|$ notation. Inserting eq. (3) into eq. (5) we arrive at

$$C_{ijkl}(\dot{\epsilon}_{kl} - \dot{\epsilon}_{kl}^p)n_j + \rho c\dot{v}_i = 0 \quad (6)$$

and finally by inserting the kinematic relation (2) into (6) and using (4) to operate on the total velocity gradient, we arrive at

$$(C_{ijkl}n_jn_l - \rho c^2\delta_{ik})\dot{v}_k + C_{ijkl}\dot{\epsilon}_{kl}^pn_jc = 0 \quad (7)$$

where \mathbf{n} is the wave normal (given as a function of two angles in spherical coordinates). Eq. (7) reduces to the

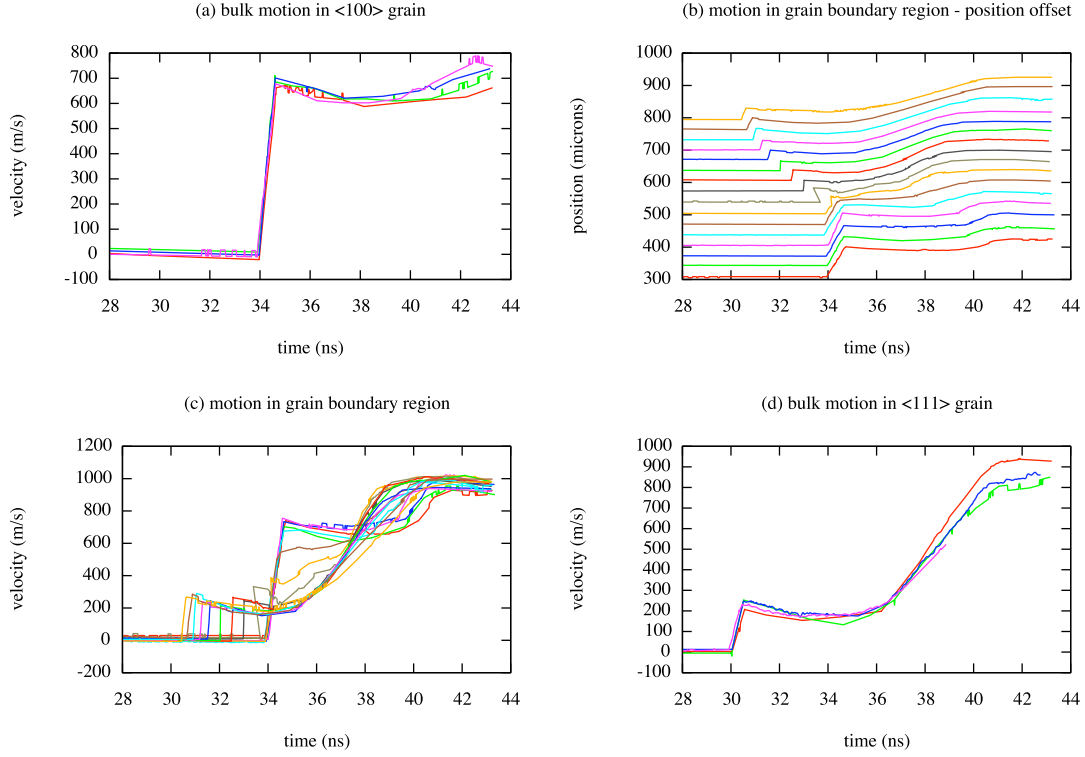


FIGURE 18. Analyzed velocity records for sample bx-04-25 showing various regions of bicrystal

standard anisotropic elastic wave equation when the plastic strain-rate is zero. This equation relates the acceleration of material points and wave speed for arbitrary directions in the crystal and a plastic strain-rate. The acceleration is related to the stress-rate through (5) and can be taken to be arbitrary or measured from a VISAR record.

The real question at hand is how plastic flow and slip hardening affect elastic-plastic wave propagation in real crystals. Two common forms of rate-dependent plastic flow laws are based on the velocity of mobile dislocations [22] and power-law hardening [25]. Both of these forms provide a shearing rate on an operative slip plane in the slip direction. The shear strain-rate can be rotated from the slip system basis (typically, the principal axes of material symmetry) to the coordinate system of the problem. The total strain-rate tensor in the problem coordinates will be a sum over slip systems of the individual strain-rates as

$$\dot{\epsilon}^p = \sum_{\beta} \mathbf{R}_{\beta}^T \dot{\epsilon}_{\beta}^p \mathbf{R}_{\beta} \quad (8)$$

The plastic strain-rate tensor in the coordinate system of each slip system has as its non-zero components half the shear strain-rate on the slip plane in the slip direction. The shearing-rate on individual slip systems is driven by the resolved shear stress on those slip systems, which can

be calculated from a VISAR record by multiplying the measured longitudinal stress by the Schmid factor. For a [111] loading direction in NiAl the slip system with the highest Schmid factor is the $\{110\}\langle 001 \rangle$ system, which has a Schmid factor of .47. The longitudinal stress at the elastic limit was calculated from the VISAR records for the [111] grain as 4.75 GPa resulting in a resolved shear stress at the moment of yielding of 2.23 GPa for primary slip. It is difficult to perform a similar calculation for the [001] grain since we do not know exactly what slip system(s) were active. We could in theory repeat the calculation for all points behind the precursor to obtain the resolved shear stress as a function of time; however, with increased plastic flow comes increased off-normal loading.

It is conceivable that eq. (7) could be used to obtain plastic flow data from velocity records by measuring the free surface velocity and wave speed continuously during an experiment and then using this data to calculate the plastic flow and hardening parameters. This would require multiple experiments along different loading directions. It would also be possible to evaluate a given plastic flow law by comparing the solution of (7) to a given experiment.

As a simplified solution to obtaining all plastic flow parameters, we attempt to calculate a single plastic shear-

strain rate of the primary slip systems for shock loading along $\langle 111 \rangle$. In this direction, there are 3 independent slip systems all with equal Schmid factors, which slip with 3-fold symmetry about the $\langle 111 \rangle$ direction. The grain orientation and slip systems are given in table 3. In table 3, the x_1 direction is the loading direction for

TABLE 3. Grain orientation and slip systems used in [111] shock calculation

	x_1	x_2	x_3
grain orientation	[111]	[11 $\bar{2}$]	[$\bar{1}$ 10]
slip systems	[001]	[110]	[$\bar{1}$ 10]
	[100]	[011]	[0 $\bar{1}$ 1]
	[010]	[101]	[10 $\bar{1}$]

the grain and the slip direction for the slip systems. x_2 is a perpendicular in-plane direction in the VISAR records for the [111] grain and is the slip plane for each slip system. x_3 was chosen as to make an orthonormal basis for each. For arbitrary directions, the slip systems are rotated and summed using eq. (8) where the only non-zero components of $\dot{\epsilon}_p^p$ are the x_1x_2 and x_2x_1 components, which both equal $\dot{\gamma}/2$ for all slip systems given the symmetry. To simplify the calculation, the stiffness tensor and the plastic strain-rate tensor are rotated into the coordinate system of the grain given in table 3. In this coordinate system we take $\mathbf{n} = \{1, 0, 0\}$ and $\dot{\mathbf{v}} = \|\dot{\mathbf{v}}\|\mathbf{n}$ where the magnitude of $\dot{\mathbf{v}}$ is obtained from the VISAR record. Immediately behind the precursor, a deceleration occurs over about 3 ns approximately equal to $2.5 \times 10^{-9} \text{ m/s}^2$, which is obtained by taking into consideration the velocity (and acceleration) doubling from the VISAR records. The wave speed in this region can be calculated from the VISAR record based on the precursor speed and the time of arrival to be roughly 6500 m/s. Using these values, we obtain $\dot{\gamma} = 7.3 \times 10^5 \text{ s}^{-1}$. Plastic strain-rates calculated in this way are probably more relevant to regions in the plastic wave in which the acceleration is positive. As the VISAR records in this research have shown, the $\langle 111 \rangle$ grains have exhibited stress relaxations (deceleration), which may be due to other mechanisms not covered in the above calculation. By applying the above calculation to the steep accelerating region of the VISAR records, we find that an acceleration of $1.95 \times 10^{10} \text{ m/s}^2$ (halved from VISAR record) and a wave speed of 5230 m/s lead to $\dot{\gamma} = -1.7 \times 10^6 \text{ s}^{-1}$.

Previous research [19, 21, 26] has primarily focused on precursor decay rather than stress relaxation processes behind the precursor. Precursor amplitude decay and stress relaxation behind the precursor may, however, be related. Two of the primary mechanisms of stress relaxation are believed to be nucleation of defects in the precursor and multiplication of dislocations by cross-slip, which neither of are considered in the above formalism. In the present study homogeneous nucleation of disloca-

tions could be responsible for the stress relaxation immediately following the precursor since this appears to be the region of highest plastic strain-rate. Following the minimum in the velocity curve, a much smoother rise to the peak velocity is observed. This is the region where plastic flow by conventional slip is believed to be taking place and is likely to obey eq. (7).

6. CALCULATIONS OF ANISOTROPIC ELASTIC-PLASTIC WAVE SCATTERING AT GRAIN BOUNDARIES

In this section we expand the scope of the equations derived in the previous section to treat the problem of elastic-plastic wave scattering in crystalline solids. The formulation of the problem is kept as general as possible by considering full anisotropic elasticity with the addition of plastic flow on all possible slip systems (in NiAl). Since there is very little previous work treating anisotropic plastic wave scattering, we attempt to build from the anisotropic elastic wave scattering theory put forth by Musgrave [1] and Auld [2]. In developing this model, we soon find out that a different solution technique from that of the elastic theory must be used since, with the inclusion of crystal plasticity, there is a departure from the eigenvalue problem of anisotropic elasticity. The elastic theory does remain useful in guiding us to the correct trends in the scattering behavior.

We begin by assuming that both quasi-longitudinal (QL) and quasi-shear (QS) waves exist (except in exceptional cases) where the definition of quasi is taken from anisotropic elasticity theory to mean that, in general, the polarization (particle motion) points in a different direction than the wave normal. We also assume the incident state is at initial yielding meaning the elastic precursor has already moved past and there is no time or space evolution (i.e. the configuration is steady). For this work, we confine ourselves to two-dimensional scattering so that the polarization and wave normal of all waves are contained in a single plane. We will find later on that, much like in the elastic theory, the two-dimensional assumption is valid only for certain orientations.

The governing (vector) equation is still eqn. (7), which remains valid for all waves. A schematic representation of the problem we wish to solve is shown in Fig. 19. Here we take

$$\mathbf{n} = \sin\phi \cos\theta \mathbf{i} + \sin\theta \sin\phi \mathbf{j} + \cos\phi \mathbf{k} \quad (9)$$

where θ represents the angle in the xy-plane. It is taken as $\pi/2$ or $3\pi/2$ for grain 2 and grain 1, respectively. We impose the continuity condition that the phase speed

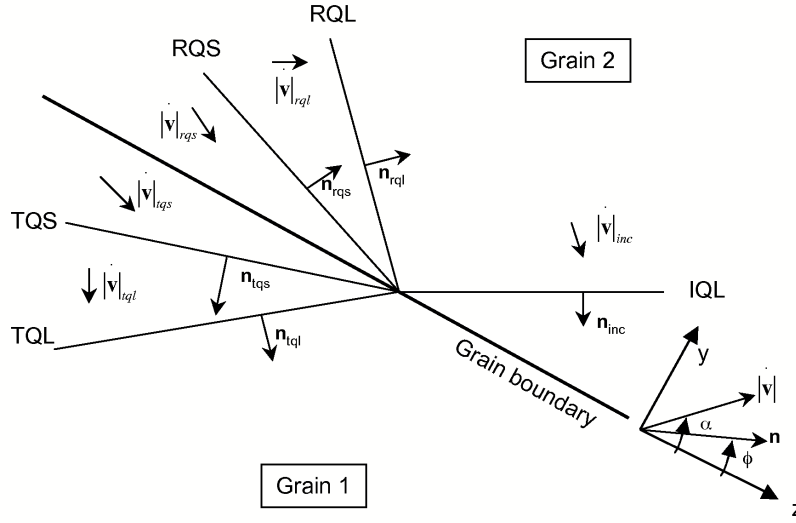


FIGURE 19. Schematic of elastic-plastic wave scattering model

along the boundary is equal for all waves

$$\begin{aligned} \frac{c_{RL,RS}}{\sin(90 - \phi_{RL,RS})} &= \frac{c_{TL,TS}}{\sin(90 - \phi_{TL,TS})} \\ &= \frac{c_{inc}}{\sin(90 - \phi_{inc})} \end{aligned} \quad (10)$$

Here, the subscripts represent reflected longitudinal, reflected shear, transmitted longitudinal, and transmitted shear waves. The orientation of the two grains is given in Fig. 3. The stiffness tensor in lattice coordinates was rotated into the grain boundary frame for each grain using $C_{ijkl} = R_{ia}R_{jb}R_{kc}R_{ld}C_{abcd}$.

The main difficulty in this formulation arises from the plastic flow, which, if we assume plastic flow by dislocation motion, prevents the problem from being one where the solutions are eigenvalues. For this reason, we must find a different method of solution, which will be discussed shortly.

The plastic strain-rate tensor is made more general here than in the previous section by putting it in terms of the symmetric part of the Schmid tensor

$$\dot{\epsilon}^p = \frac{1}{2} \sum_{\beta} \dot{\gamma}^{(\beta)} (\mathbf{b} \otimes \mathbf{m} + \mathbf{m} \otimes \mathbf{b}) \quad (11)$$

This plastic strain-rate tensor is then rotated into the problem coordinates of the grain boundary so that eqn. (7) may be used. The slip planes and vectors used in eqn.

TABLE 4. Available slip systems in NiAl

slip vector	slip plane
[100]	(01 $\bar{1}$)
	(011)
	(010)
	(001)
[010]	(10 $\bar{1}$)
	(101)
	(100)
	(001)
[001]	(1 $\bar{1}$ 0)
	(110)
	(100)
	(010)

(11) are given in table 4. The $\dot{\gamma}$ for each slip system is often given in terms of a rate sensitivity parameter as in [25]. Here we have neglected this form knowing that the same procedure could be used for different plastic constitutive relations and simply used the form

$$\dot{\gamma}^{(\beta)} = \dot{a} \frac{\tau_{RSS}}{\tau_{CRSS}} \quad (12)$$

where \dot{a} is the shearing rate at initial yielding (taken to be $1 \cdot 10^5 \text{ s}^{-1}$), a subscript RSS represents the resolved shear stress on a slip system, and CRSS represents the

critically resolved shear stress on a slip system. In calculating the $\dot{\gamma}^{(\beta)}$, we have allowed for both forward and backward slipping by taking the sign of the Schmid factor. In most crystal plasticity formulations, the critically resolved shear stress will vary with deformation according to some hardening law. In keeping with the steady-state nature of this model, we assume the hardening to be nonexistent and simply take τ_{CRSS} to be 2.23 GPa as given in the previous section. The resolved shear stress is given by

$$\tau_{RSS} = \sigma * S.F. \quad (13)$$

where σ ($= 1$ initially) is the magnitude of stress and S.F. is the Schmid Factor. The load (unit) vector used in calculating the Schmid factor being parallel to the particle acceleration (and traction) vector by eqn. (5) is taken to be a function of the angle α . By doing this, we can put $\dot{\epsilon}^p$ in terms of the angle α , which is a key part of the solution technique discussed below. Figs. 20 and 21 show how the Schmid factors vary with direction in the [001] grain and [111] grain respectively where [001] is grain 1 in Fig. 19. From the form of the curves in

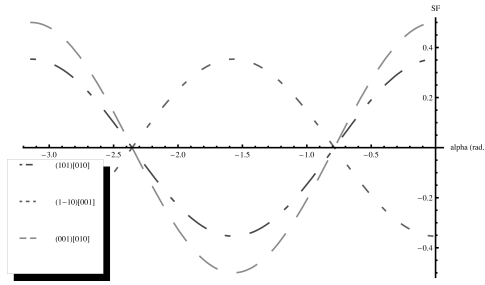


FIGURE 20. Variation of Schmid factors with respect to loading direction for the [001] grain

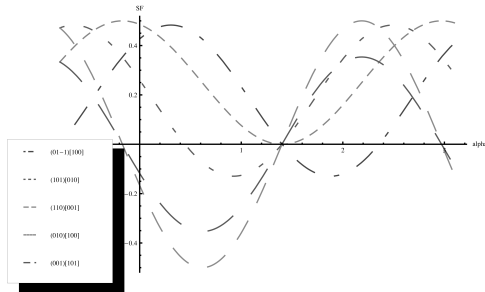


FIGURE 21. Variation of Schmid factors with respect to loading direction for the [111] grain

Figs. 20 and 21 we can make a few observations about the directionality of plastic flow in each grain. Firstly, for the [001] grain, the plastic strain rate tensor only has non-zero components, which are equal and opposite, in the yy and zz positions. This arises due to the fact that two pairs of slip systems cancel each other as can be seen from Fig. 20 leaving only two equivalent systems to control plastic flow in the plane. This differs significantly from the [111]

grain where all plastic strain-rate tensor components are non-zero resulting in much less constrained behavior when we calculate the particle acceleration vector.

The governing equation that we are using, eqn. (7), represents a circular argument since in order to solve it we need to know σ and the direction of the load vector given by α . We circumvent this problem by setting σ initially to 1 and stepping over discrete values of α from 0 to π for single discrete values of ϕ . (The α 's n and $n+\pi$ produce the same solution.) The angle ϕ is then looped over from 0 to $\pi/2$. Furthermore, since we are not currently interested in looking for all possible solutions of varying wave normals, acceleration vectors, and wave speeds, we can use eqn. (10) in place of c in eqn. (7), which makes c a function of ϕ , to only look for solutions that satisfy eqn. (10). The acceleration vector (for each wave) is then calculated by

$$\dot{v}_k = -[C_{iakk}n_a n_b - \rho c^2 \delta_{ik}]^{-1} C_{idef} \epsilon_{ef}^p n_{dc} \quad (14)$$

A valid solution is when $\dot{v}/||\dot{v}||$ points in the same direction as the α used to calculate it. Since σ is simply a scalar that can be factored out (or set to unity), it does not change the determination of the direction of the acceleration vector, only its magnitude. Also, we look for both \dot{v} and $-\dot{v}$ solutions since the sign of σ will reverse the direction of the calculated acceleration vector. In order to find both QL and QS waves, we have made the classification that a QL wave is one where the acceleration vector is within $\pm 45^\circ$ from the wave normal and a QS wave is one where it is greater than 45° from the wave normal. Finally, we refine the step size in both α and ϕ until the calculation converges onto solutions that satisfy a constraint, namely when the vector defined by α is within a small angle of the calculated solution, $\dot{v}/||\dot{v}||$.

For these calculations, we define the incident wave to be in grain 2 and to have a σ of 5 GPa (compressive) and wave normal and acceleration vector to both be pointing in the [111] direction. By eqn. (14) we calculate the wave speed for these values to be 7000 m/s. This is a higher velocity than expected (or measured) most likely due to the fact that in reality, the acceleration vector probably does not point exactly in the [111] direction. We found that if we used the measured value of 5230 m/s for the incident plastic wave velocity, considerable out-of-plane acceleration vector components arose. To keep the calculations two-dimensional, we have used 7000 m/s for the incident wave velocity and assumed that the other wave speeds in the calculation would be high since they are based on this value.

Leaving the scattering problem for a moment, one important aspect of the general anisotropic elastic-plastic behavior is to find how the wave speed, particle acceleration, and wave normal depend on each other. To find this behavior we decided to vary the wave speed within each

α (and thus ϕ). For a single α we found that in the $\langle 100 \rangle$ grain, the wave speed increased with increasing α . Some angles of the acceleration vector did not give a solution for any wave speed. At larger wave normal angles, the increase in wave speed with α was more rapid. More study concerning these dependencies is required including the dependence of applied stress on wave speed, which should add an additional level of difficulty.

Returning to the scattering problem, by stepping through α for each ϕ , we find that multiple solutions may exist for a single incident wave state. This is initially disconcerting, however, since we are not yet imposing (or determining) the stress jump across each wave (which could be compressive or tensile in nature) it could be that some solutions represent elastic solutions and some represent continued plastic deformation.

Specifically, we find for both grains that low wave normal (fast wave) solutions exist for both QL and QS waves, which would be representative of elastic waves. For grain 1 ($[001]$), the wave normals for low angle QL waves point inside of about 20° from the boundary and for grain 2 they point inside about 30° from the boundary. Low angle shear waves also exist and occur near 40° in grain 1. For grain 2, the low angle shear waves appear to be very near the longitudinal ones. In the case of grain 2 only, for higher angle wave normals and acceleration vectors, increasingly large out-of-plane components develop for particle motion, which increases our error in assuming a two-dimensional problem. We have set a bound on the magnitude of the out-of-plane component before we begin to ignore these solutions. This is probably the main reason the low angle QS waves are very near the low angle QL waves for grain 2.

High angle wave normal solutions exist as well and occur near 53° and 75° for QL and QS waves in grain 1, respectively. For grain 2, only high angle solutions exist for QL waves given the constraint set on out-of-plane motion. This angle being 48° from the boundary.

For both grains 1 and 2, the acceleration vectors associated with the low angle solutions point in the same general direction as the wave normal whereas the high angle solutions point towards the opposite direction. Remembering that we used a value of 1 for σ , if the calculated σ is negative, then the actual acceleration vector will be in the opposite sense as that calculated in the above.

To find the true configuration including angles, velocities, and stresses behind all reflected and transmitted waves, we must use the conditions of equivalence of acceleration and traction-rate across the grain boundary. The conditions at the boundary are summarized as

$$\begin{aligned} \sigma_{inc} \dot{\mathbf{v}}|_{inc} + \sigma_{rqs} \dot{\mathbf{v}}|_{rqs} + \sigma_{rql} \dot{\mathbf{v}}|_{rql} \\ = \sigma_{tqs} \dot{\mathbf{v}}|_{tqs} + \sigma_{tql} \dot{\mathbf{v}}|_{tql} \end{aligned} \quad (15)$$

and

$$\begin{aligned} \sigma_{inc} c_{inc} |\dot{\mathbf{v}}|_{inc} + \sigma_{rqs} c_{rqs} |\dot{\mathbf{v}}|_{rqs} + \sigma_{rql} c_{rql} |\dot{\mathbf{v}}|_{rql} \\ = \sigma_{tqs} c_{tqs} |\dot{\mathbf{v}}|_{tqs} + \sigma_{tql} c_{tql} |\dot{\mathbf{v}}|_{tql} \end{aligned} \quad (16)$$

where subscripts inc, rql, rqs, tql, and tqS represent incident, reflected quasi-longitudinal and shear, and transmitted quasi-longitudinal and shear. Note that the density has dropped out of eqn. (16). Eqns. (15) and (16) are four conditions (in two-dimensions) that can be solved for the four stress magnitudes of the reflected and transmitted waves. These are actually the magnitudes of the stress jumps and not absolute values since they come from the jump in $\dot{\gamma}^{(\beta)}$.

Since we have (presumably) two possible solutions for each wave we need to look at a few possible combinations of these solutions to determine the correct one. For simplicity, assuming the QL and QS waves have the same behavior within each grain, we will look at four configurations. These configurations fall under the following categories: elastic-elastic, plastic-elastic, plastic-plastic, or elastic-plastic transitions from grain 2 to grain 1. When looking at possible elastic-elastic and plastic-elastic transitions, we immediately find that the predicted stresses are two orders-of-magnitude too high from the value we gave to the incident wave (5 GPa). Also, since for elastic (release) waves, the acceleration vector associated with each should point in the opposite direction of the wave normal, which they do not in the case of the elastic-elastic configuration. In the case of the plastic to plastic transition, the acceleration vector for grain 2 points in the direction of tension, which again would signify an elastic release wave instead of a compressive plastic wave.

The elastic to plastic transition appears to be the only one that adheres to the expected properties of scattered elastic and plastic waves. The elastic RQL wave has a magnitude of 2 GPa and points in the direction of tension 205° from the z-axis. The TQL wave has a magnitude of 9 GPa and points in the compressive direction 56° from the z-axis in the $-\alpha$ direction. The effect of the QS waves are more difficult to understand since they cannot immediately be shown to be in one direction or the opposite based on whether the wave is elastic or plastic.

7. DISCUSSION AND CONCLUSIONS

A number of results may be deduced from the above VISAR data as already shown with the flow stress (3.3 and 2.9 GPa for $\langle 100 \rangle$ and $\langle 111 \rangle$ crystals respectively). The velocity profiles in the bulk of the $\langle 111 \rangle$ grain showed a smoothly varying rise (following stress relaxation) to the peak velocity in the plastic wave. For the

few samples shocked above the elastic limit in the $\langle 100 \rangle$ grain, unstable $\langle 100 \rangle$ slipping was observed in the form of a jagged rise to the peak velocity. This appears to be nice evidence that the "kinking" mechanism observed in quasi-statically loaded $\langle 100 \rangle$ NiAl single crystals is still active under shock conditions.

Depending on whether or not one or both grains was shocked above the elastic limit, various lateral transitions across the grain boundary were observed from the VISAR records, which connected the elastic precursors and plastic waves. These transitions were mostly smooth and arose due to the (linearly) increasing amount of time that the precursor spent in one grain relative to the other as it propagated through the thickness. VISAR records showing plastic waves in both grains also show a similar transition between the plastic wave fronts, which were slightly harder to detect.

Extreme velocity gradients were observed across the point where the grain boundary intersected the free surface on the $\langle 100 \rangle$ grain side. These velocity gradients persisted from the time of arrival of the $\langle 100 \rangle$ precursor until the $\langle 111 \rangle$ plastic wave arrived in the grain boundary region. This also tells us why these large gradients formed since at this time we have large particle velocities in the $\langle 100 \rangle$ precursor and immediately adjacent to these points across the boundary, we have plastic flow occurring due to the $\langle 111 \rangle$ orientation, which has a considerably lower particle velocity as seen by the VISAR records. Elastic-elastic, plastic-elastic, and plastic-plastic transitions were expected to occur across the grain boundary, although clear evidence of these transitions could not be seen in the VISAR records.

Calculations were performed to extract plastic strain-rate data on specific slip systems using free surface velocity data. The derived equations seem to be best suited for regions of acceleration behind the precursor otherwise they predict that the plastic strain-rate will reverse sign if stress-relaxation is present. The stress-relaxation region is probably better described by a dislocation nucleation and/or multiplication model. Measurements of in-plane velocities would allow an improved prediction of additional plastic flow properties.

The region affected by the presence of the grain boundary was shown to be larger by tens of μm than the projection of the boundary on the free surface. This appears to be evidence of elastic-plastic wave scattering off of the inclined boundary. A model was developed to treat this problem considering full crystal elasticity and plasticity. Two sets of solutions were found to be possible for each wave, one corresponding to an elastic wave and one corresponding to a plastic wave. The two solutions for each wave occurred at low wave normal angles (relative to the boundary) characteristic of a fast moving elastic wave and at high wave normal angles characteristic of a slower moving plastic wave. For this model,

we assumed that the state ahead of the incident wave is on the yield surface so that all elastic waves must correspond to release waves and scattered plastic waves must be associated with an additional jump in stress and particle acceleration in the direction of the propagating wave. For the case of an incident wave propagating along a $\langle 111 \rangle$ direction contained in a 110 plane and scattering off a 45° inclined boundary separating a $\langle 100 \rangle$ shock direction grain, we find that the model predicts reflected elastic release waves and transmitted plastic compression waves.

We found that greater errors are introduced due to our two-dimensional approximation for higher wave normal and acceleration vector angles since at these high angles, out-of-plane components must arise in the $\langle 111 \rangle$ grain. Furthermore, we only considered four possible configurations: elastic-elastic, plastic-elastic, plastic-plastic, and elastic-plastic for the reflected and transmitted states across the boundary. It is very likely that the states behind a QL and QS wave may not be the same, which we did not consider. This will require coming up with a more efficient way to look at all possible combinations to choose the correct one. We could not repeat the same calculation for $\langle 100 \rangle$ to $\langle 111 \rangle$ transitions across a grain boundary due to the fact that, plastic waves cannot be propagated in the $\langle 100 \rangle$ direction in NiAl unless there is another mechanism available for plastic flow.

ACKNOWLEDGMENTS

The authors would like to thank Ken McClellan and Darrin Byler of MST-8 (LANL) for the use of the crystal growth lab and instruction. This work was performed under LANL LDRD-DR- principal investigator, Aaron Koskelo.

REFERENCES

1. M.J.P. Musgrave, Reports on Progress in Physics 22: 74-96, 1959.
2. B.A. Auld, Acoustic Fields and Waves in solids, Robert E. Krieger publishing, 1990 (2nd ed.).
3. E. Loomis, P. Peralta, D. Swift, accepted JEMT, 2007.
4. D.L. Paisley, D. Swift, A.C. Forsman, G.A. Kyrala, R.P. Johnson, R.A. Kopp, A.A. Hauer, J.S. Wark, A. Loveridge, A. Allen, D.H. Kalantar, High Power Laser Ablation III, Proceedings of SPIE, 4065: 482-489, 2000.
5. A. Loveridge-Smith, A. Allen, J. Belak, T. Boehly, A. Hauer, B. Holian, D. Kalantar, G. Kyrala, R.W. Lee, P. Lomdahl, M.A. Meyers, D. Paisley, S. Pollaine, B. Remington, D.C. Swift, S. Weber, J.S. Wark, Physical Review Letters, 86 (11): 2349-2352, 2001.
6. D.C. Swift, D.L. Paisley, G.A. Kyrala, A. Hauer, AIP conference in Shock Compression of Condensed Matter-2001, p. 1192.

7. J.W. Craggs, J. Mech. Phys. Solids 5: 115-124, 1957.
8. T.C.T. Ting, N. Nan, JAP: 189-197, 1969.
9. B.D. Reddy, T. Gültop, Eur. J. Mech. A/Solids 14 (4): 529-551, 1995.
10. J.C. Cizek, T.C.T. Ting, JAM 45: 51-59, 1978.
11. W.E. Jahsman, JAM: 117-123, 1974.
12. D.B. Miracle, Acta Metall. Mater. 41 (3): 649-684, 1993.
13. R.D. Noebe, R.R. Bowman, M.V. Nathal, Int. Mater. Rev. 38 (4): 193-254, 1993.
14. D.B. Miracle, Acta Metall. Mater., 39 (7): 1457-1468, 1991.
15. S.A. Maloy, G.T. Gray III, R. Darolia, Mater. Sci. Eng. A A192/193: 249-254, 1995.
16. D.R. Greening and A. Koskelo, APS proceedings-Shock Compression of Condensed Matter, 2003.
17. Zel'dovich and Raizer, Physics of Shock waves and high temperature hydrodynamic phenomena, Dover, New York, 1967.
18. D.C. Swift, Los Alamos Unclassified Report, LA-UR-05-1223, 2005.
19. J.J. Dick, G.E. Duvall, J.E. Vorthman, JAP 47 (9):3987, 1976.
20. J.R. Asay, G.R. Fowles, Y. Gupta, JAP 43 (2): 744, 1972.
21. J.N. Johnson, O.E. Jones, T.E. Michaels, JAP 41 (6): 2330, 1970.
22. J.N. Johnson, JAP 43 (5): 2074-2082, 1972.
23. R. Hill, J. Mech. Phys. Solids 10: 1-16, 1962.
24. D.M. Janssen, S.K. Datta, W.E. Jahsman, J. Mech. Phys. Solids 20: 1-18, 1972.
25. D. Peirce, R.J. Asaro, A. Needleman, Acta Metall. 31 (12): 1951-1976, 1983.
26. Y.M. Gupta, JAP 46 (8):3395-3401, 1975.

This work performed under the auspices of the U.S. Department of Energy by Lawrence Livermore National Laboratory under Contract DE-AC52-07NA27344.